

Phase diagram of the disordered Kitaev chain with long-range pairing connected to external baths

Emmanuele G. Cinnirella^(1,2), Andrea Nava⁽³⁾, Gabriele Campagnano⁽⁴⁾, and Domenico Giuliano^(1,2)

⁽¹⁾*Dipartimento di Fisica, Università della Calabria Arcavacata di Rende I-87036, Cosenza, Italy*

⁽²⁾*INFN, Gruppo collegato di Cosenza, Arcavacata di Rende I-87036, Cosenza, Italy*

⁽³⁾*Institut für Theoretische Physik, Heinrich-Heine-Universität, 40225 Düsseldorf, Germany*

⁽⁴⁾*CNR-SPIN, c/o Complesso di Monte S. Angelo, via Cinthia - 80126 - Napoli, Italy*

(Dated: April 16, 2025)

We study the phase diagram of a disordered Kitaev chain with long-range pairing when connected to two metallic leads exchanging particles with external Lindblad baths. We (i) monitor the subgap modes at increasing disorder, (ii) compute the current flowing across the system at a finite voltage bias between the baths, and (iii) study the normal single particle lead correlations across the chain. Throughout our derivation, we evidence the interplay between disorder and topology. In particular, we evidence the reentrant behavior of the massive, topological phase at limited values of the disorder strength, similar to what happens in the short-range pairing Kitaev model. Our results suggest the possibility of a disorder-induced direct transition between the massive and the short-range topological phase of the long-range pairing Kitaev model.

I. INTRODUCTION

In the pursuit for systems with excitations suitable for quantum computation purposes, quantum topological systems have gained constantly increasing importance. The main feature of a quantum topological phase is the emergence of states localized at the boundary of the system which can only be removed by letting the system undergoing a topological phase transition[1, 2]. Such boundary states in one dimensional (1D) systems have been proposed to be useful in quantum computation protocols in several platforms, such as quantum Hall states at filling 5/2 [3, 4], helical states in electron liquids [5], or in photonic metamaterials [6] to mention a few.

A topological phase can be identified by a topological invariant such as the Chern number \mathcal{C} —the integral of the Berry curvature over the Brillouin zone of the system with periodic boundary conditions [7]. Typically, \mathcal{C} is quantized and, due to the bulk-boundary correspondence[8–10], its value, computed in the translationally invariant system with periodic boundary conditions, corresponds to the number of edge modes emerging at the boundaries of the system with open boundary conditions. In models with short-range interactions and/or electron hopping $|\mathcal{C}| = 0$ or 1, respectively in the topologically trivial or nontrivial phases. At variance, an hopping beyond nearest neighbors can stabilize phases with $|\mathcal{C}| > 1$, corresponding to multiple, independent, exponentially localized topological zero energy modes at the boundary of the system. Remarkably, this behavior, theoretically predicted for both normal [11–14], and superconducting systems [15–18], has recently been experimentally observed in optical lattice simulations of topological systems [19, 20].

On the other hand, many experimental systems able to host topological phases of matter, such as Rydberg synthetic lattices [21–23], optical waveguides [24, 25], and trapped ions [26], exhibit power-law decaying interactions. Most relevant to our work, power-law decaying

interactions have been studied in the Kitaev chain with long-range tunneling and/or pairing hopping (LRK) [27–29] and in the helical Shiba chain [30, 31], concerning both static and dynamical properties in the presence of quenches [32–35], or periodic drivings [36, 37], as well as the investigation of the entanglement entropy growth [38, 39]. Such interactions are expected to lift the degeneracy of the zero energy modes, giving rise to massive subgap topological states characterized by a finite energy, a wavefunction showing a power law spatial decay inside the bulk and a noninteger value of the topological invariant [40–43].

In this work we address the phase diagram of the LRK in the presence of disorder. In 1D normal systems, any amount of disorder is known to fully localize the electronic wavefunctions, thus inducing a transition toward a disorder-induced insulating phase [44–46]. At variance, in topological systems a limited amount of disorder may work to enforce the topological state, thus leading to a reentrant topological phase [47–51], till it becomes strong enough to induce a phase transition to trivial phases. A reentrant topological phase is, by now, a well-established feature of 1D disordered, topological superconductors [47, 52, 53]. In the specific context of the LRK model, previous studies of the effects of disorder have concerned a closed system with a discommensurate one-particle potential term [54] or a correlated commensurate one [55], or the nonequilibrium dynamics following a parametric quench of the model Hamiltonian [56, 57].

In general, disorder makes it difficult to even define \mathcal{C} , except in remarkable situations, where additional symmetries allow for consistently computing it [49, 50, 58–62]. Thus, when investigating the combined effects of disorder and topology on the phase diagram of the system, it is worth resorting to alternative means to set the boundaries of topological phases. In this direction, in Refs.[50, 51] we proposed to employ the even-odd differential occupancy of the lattice sites, combined with a systematic analysis of the transport properties of the sys-

tem, taken to a non-equilibrium steady state (NESS) by means of a coupling to an external dissipative (Lindblad) bath. Indeed, a direct coupling to the external bath has already proven to be an effective tool to study the phase diagram of topological 1D systems [50, 51], as well as the onset of topological dynamical phase transitions in two dimensional superconducting systems [63, 64], and to detect the presence of non-trivial physical behaviors like the Mpemba effect [65, 66], the dynamical parity stabilization [67, 68] or the dissipative cooling [69]. Along this line, here we study the phase diagram of an open LRK with Anderson disorder [27, 28, 70], connected to 1D metallic leads and allowed to exchange particles with a Lindblad bath at a given chemical potential [71, 72].

Specifically, we implement three different means of identifying the various phases of the disordered LRK: (i) we look at the lowest and at the next-to-lowest energy mode of the isolated chain, (ii) we monitor the current \mathcal{I} across the LRK, and (iii) the single-particle lead correlations across the LRK, $C_{L,R}$ in the NESS, when the baths are taken at a finite voltage bias, as a function of both the potential bias between the baths and the disorder strength. Our approach is grounded on the different structure of the subgap modes in the various phases of the LRK in the absence of disorder. Indeed, as we review in the following, the model shows a trivial phase, with no energy modes below the bulk gap, a topological phase, equivalent to the one of the Kitaev model [73], with two degenerate, real fermionic modes pinned at zero energy (for a long enough chain), and a “topological massive phase”, with a finite-energy subgap mode, which can be regarded as being determined by an overlap between the real fermionic modes that keeps finite in the infinite chain limit [27, 28, 70]. Doing so, we evidence the robustness of the nontrivial phase with a finite energy subgap mode (a typical feature of the LRK [74–76] which is related to the possibility, for the LRK, to work as an efficient “particle entangler”, by means of a mechanism dual to the crossed Andreev reflection across the Kitaev chain [70]) against Anderson disorder.

Throughout our derivation, we first show how to identify the various phases of the LRK in the absence of disorder by looking at the low-lying energy modes of the system, at \mathcal{I} and at $C_{L,R}$. Then, we compute them in the presence of disorder and monitor up to which value of the disorder strength a feature characterizing a given phase survives (which is a signal that the corresponding phase is still surviving the disorder), setting the corresponding phase boundary at the point where the feature itself disappears. In this way, we are able to map out the phase diagram of our system. Eventually, we verify that the results independently obtained by looking at the three quantities are all consistent with each other.

Our paper is organized as follows:

- In Sec. II, we present the model Hamiltonian for the LRK in the absence of disorder and briefly review its phase diagram. Then, after adding Anderson disorder, we look at the two lowest-lying energy

eigenvalues to argue how, and to what extent, the disorder modifies the phase diagram, with respect to the clean limit.

- In Sec. III, we introduce the Lindblad master equation approach to the LRK coupled to two external leads exchanging particles with Lindblad baths at different potentials and recover the formulas for computing \mathcal{I} and $C_{L,R}$ in the NESS.
- In Sec. IV, we study the behavior of the current and of the modulus of the endpoint correlations between the metallic leads in the NESS and relate it to the various phases of the disordered LRK.
- In Sec. V, we summarize our main conclusions and present possible further developments of our work.
- In Appendix, we provide mathematical details of the formalism of Lindblad Master Equation that we employ throughout our derivation.

II. MODEL HAMILTONIAN

In the following, we review the model Hamiltonian and the phase diagram of the isolated LRK, first in the clean limit, and then at nonzero disorder strength.

A. The long-range Kitaev chain in the absence of disorder

The LRK describes spinless fermions over a one-dimensional (1D) lattice, with a nearest neighbor normal hopping strength w and a p -wave, superconducting pairing term decaying, in real space, as a power of the distance between two sites. Over an L -site chain, the LRK Hamiltonian H is given by [27, 70, 75, 77]

$$H = -w \sum_{j=1}^{L-1} \left(\chi_j^\dagger \chi_{j+1} + \chi_{j+1}^\dagger \chi_j \right) - \mu \sum_{j=1}^L \chi_j^\dagger \chi_j + \frac{\Delta}{2} \sum_{j=1}^{L-1} \sum_{r=1}^{L-j} \delta_r^{-\alpha} \left(\chi_j^\dagger \chi_{j+r}^\dagger + \chi_{j+r} \chi_j \right). \quad (1)$$

In Eq. (1) χ_j (χ_j^\dagger) are the annihilation (creation) operator for a spinless fermion at site j of the chain. They satisfy the standard anticommutation relations $\{\chi_j, \chi_{j'}^\dagger\} = \delta_{j,j'}$, $\{\chi_j, \chi_{j'}\} = \{\chi_j^\dagger, \chi_{j'}^\dagger\} = 0$. w is the single-fermion hopping strength between nearest-neighboring sites, μ is the chemical potential, Δ is the pairing strength and $\delta_r = |r|$ if $j + r \leq L$, otherwise $\delta_r = 0$. The exponent α determines the “effective range” of the interaction. $\alpha \rightarrow \infty$ corresponds to the “standard” Kitaev model, with p -wave pairing between nearest-neighboring sites over the lattice [73]. In the following, for the sake

of simplicity (and without loss of generality), we set $\Delta = 2w = 1$, to reduce the number of parameters. Switching to momentum basis and employing Nambu spinor representation, we rewrite H in Eq. (1) as

$$H = \sum_k [\chi_k^\dagger, \chi_{-k}] [\vec{h}_{\alpha,\mu}(k) \cdot \vec{\sigma}] \begin{bmatrix} \chi_k \\ \chi_{-k}^\dagger \end{bmatrix}, \quad (2)$$

with $\chi_k = \frac{1}{\sqrt{L}} \sum_{j=1}^L e^{ikj} \chi_j$, $\vec{\sigma}$ being the Pauli matrices, and [75, 77]

$$\vec{h}_{\alpha,\mu}(k) \cdot \vec{\sigma} = \begin{bmatrix} -\cos(k) - \mu & -if_\alpha(k + \pi) \\ -if_\alpha(k + \pi) & \cos(k) + \mu \end{bmatrix}, \quad (3)$$

with $f_\alpha(k) = \sum_{r=1}^{L-1} e^{ikr} / \delta_r^\alpha$. The model Hamiltonian in Eq. (1) belongs to the BDI class of the topological insulators and superconductors [78]. Its (bulk) quasiparticle spectrum is determined by the dispersion relation $E_k = \sqrt{(\cos(k) + \mu)^2 + |f_\alpha(k)|^2}$. Out of the critical lines E_k takes a finite gap E_Δ , which corresponds to the orange, solid line in Fig. 1(b).

The topological phases of an Hamiltonian in the form of Eq. (2) is typically signaled by a nonzero value of the winding number ω (which, in 1D systems coincides with C), given by [79]

$$\omega = \frac{i}{\pi} \int_{\text{BZ}} dk \langle u_k | \partial_k | u_k \rangle, \quad (4)$$

with $|u_k\rangle$ being the negative-energy eigenstate of $h_{\alpha,\mu}(k)$, and the integral performed over the full Brillouin zone [80]. In the case of a short-range Hamiltonian, ω measures how many times $\vec{h}_\alpha(k)$ revolves around the origin as k spans the whole Brillouin zone and, therefore, it can only take integer values. In our specific cases, we point out that, for $\alpha < 1$, the function $f_\alpha(k)$ in Eq. (3) has a singularity for $k = 0$, which gives rise to a third, “intermediate” phase, in addition to the trivial and to the topological one of the Kitaev model [74, 76, 81], as well as of crossover regions, corresponding to the hatched areas of Fig. 1(a). In the crossover regions ω is ill defined, thus losing its direct connection with the topological properties of the phase (see Ref.[81] for a detailed discussion of this point).

In Fig. 1(a) we draw the phase diagram of the LRK in the μ - α plane. In particular, we identify:

- **For $\alpha > 3/2$ and $|\mu| < 1$** , a topologically nontrivial phase [green region of Fig. 1(a)], corresponding to the topological phase of the short-range Kitaev model and, as such, characterized by the winding number $\omega = 1$. In this phase the system exhibits a gapped spectrum and a pair of real-fermionic zero modes localized at the endpoints of the chain, whose overlap is exponentially suppressed with the length of the chain itself.

- **For $\alpha > 3/2$ and $|\mu| > 1$** , a topologically trivial phase [grey regions of Fig. 1(a)], with $\omega = 0$, corresponding to the trivial phase of the short-range Kitaev model [77]). In this phase the system is gapped and no edge state is present.
- **For $\alpha < 1$ and $\mu > 1$** [blue region of Fig. 1(a)], there are no subgap topological states, which makes this region similar to the trivial one, for what concerns its topological properties [76].
- **For $\alpha < 1$ and $\mu < 1$** [red region of Fig. 1(a)], the system is gapped with localized real fermionic modes at the edges. Differently from the topological phase, now there is a finite overlap between the isolated edge modes, decaying as a power-law of the length of the chain. Accordingly, they hybridize and give rise to massive excitations and, at the same time, one gets a noninteger winding number $\omega = 1/2$, as a consequence of the singularity in both the dispersion relation and in the group velocity [76]. In the following we refer to this phase as to the “massive topological phase.”
- **For $1 < \alpha < 3/2$ and $|\mu| < 1$** [hatched green area of Fig. 1(a)], there is still a subgap, zero energy modes. However, the winding number is ill defined, due to the divergence of the group velocity at $k = 0$ [76].
- **For $1 < \alpha < 3/2$ and $\mu < -1$** [hatched reddish area of Fig. 1(a)], the behavior of the system is the same as in the above region, except that the subgap mode is now massive.
- Finally, for **For $1 < \alpha < 3/2$ and $\mu > 1$** [shaded grey area of Fig. 1(a)], the system undergoes a crossover between two phases, both topologically trivial.

B. The disordered long-range Kitaev chain

To introduce impurity disorder, we add to the chemical potential μ a random, site-dependent additional term ϵ_i , that is, we set $\mu_i = \mu \rightarrow \mu_i = \mu + \epsilon_i$, with $\{\epsilon_i\}$ being random numbers, distributed according to the probability distribution

$$P[\epsilon] = \begin{cases} \frac{1}{2\sqrt{3}W} & \text{if } |\epsilon| \leq \sqrt{3}W \\ 0 & \text{otherwise} \end{cases}, \quad (5)$$

and the “disorder strength” $W(> 0)$ defined so that W^2 corresponds to the variance of $P[\epsilon]$. Disorder, as we introduce it, breaks the lattice translational invariance. Thus, being able to provide a generalization of the winding number to the disordered case is, in general, no longer simple and typically depends on the specific system one

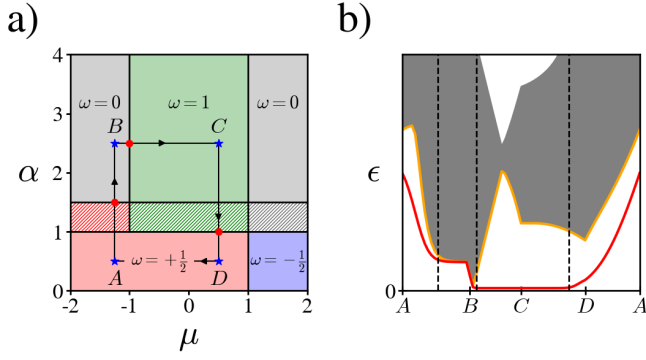


FIG. 1. (a): Phase diagram of the LRK described by H in Eq. (1) with $2w = \Delta = 1$ and $L = 500$, drawn in the μ - α plane. The various colors identify phases with different values of ω (see the main text for details). Hatched areas correspond to crossover regions, where the winding number interpolates between the adjacent regions. The red dots mark the transition points between phases with distinct topological properties.

(b): Spectrum of H along the curve $A \rightarrow B \rightarrow C \rightarrow D \rightarrow A$ highlighted in (a), with $\mu_A = \mu_B = -1.25$, $\mu_C = \mu_D = 0.5$, $\alpha_A = \alpha_D = 0.5$ and $\alpha_B = \alpha_C = 2.5$. The solid red line corresponds to the lowest energy level, the grey filled areas represent window of allowed bulk energy levels, the solid orange line corresponds to the value of the gap E_Δ , the dashed black lines highlight the crossing from one phase to another, signaled by the red dots in (a).

is considering [47, 50, 82]. For this reason, to identify the various phases of the system, in the following we look at how disorder itself affects the subgap modes in the LRK spectrum, motivated by our above observation that the various phases can be identified by monitoring those modes and how their energies behave as a function of the system parameters [70, 75]. We first compute the energies of the first two low-lying levels of the system at a given value of the system parameters and for a fixed configuration of disorder, then we average over the disorder realizations, generated by using the probability distribution in Eq. (5). To double check whether we recover a faithful description of the disordered system, we also compute the standard deviation of the energies from the average. Doing so as a function of the disorder strength W , we recover the plots shown in Fig. 2.

There, we plot, with two shaded red and grey curves, the disorder averaged value of the lowest and of the next to lowest single particle energies as a function of W , computed at the points A, B, C, and D in parameter space highlighted in the plots in Fig. 1. Moreover, the shaded width of both curves measures the standard deviation of the energies around their average value. As long as the shaded curves do not overlap with each other, we assume that the integrity of the levels is preserved. Apparently, up to $W \approx 1$, we see that the various phases are not sensibly affected by disorder. On further increasing W , the system enters a disorder dominated phases, whose specific features depend on the corresponding phase in the

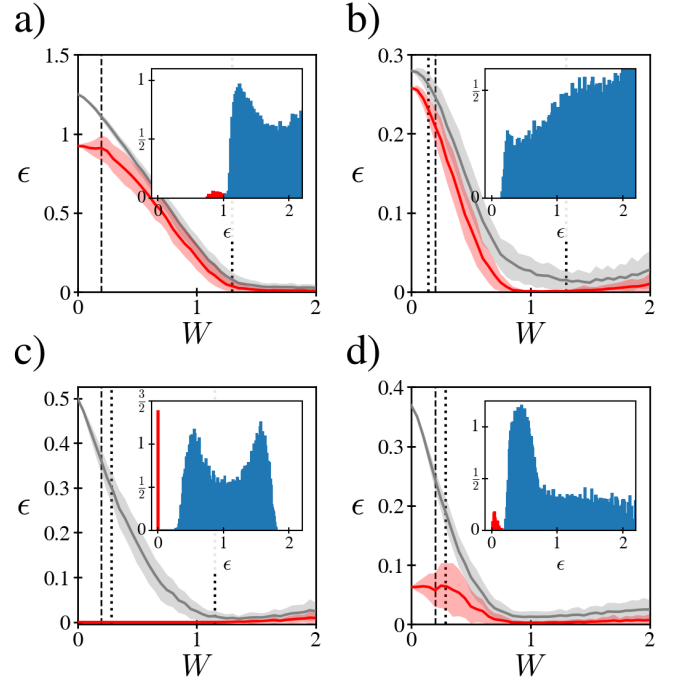


FIG. 2. Lowest energy (red line) and next to the lowest energy levels (grey line) for the disordered LRK as function of the disorder strength W corresponding to the point A (a)), B (b)), C (c)) and D (d)) of Fig. 1. The plots have been drawn for $L = 500$ by averaging over 100 different disorder configurations for each fixed W . The shaded regions measure the corresponding standard deviation at a given W . Inset plots: numerical energy density of the full spectrum in the range $\epsilon \in [0, 2]$, computed using the same disorder configurations of the main plots, at the value of W corresponding to the black dashed lines in the main plots, with the peaks corresponding to the subgap modes highlighted in red.

clean limit. Specifically, if, in the clean limit, the system is in the topologically trivial phase [Fig. 2(b)], increasing the disorder pushes the lowest, single-particle energy toward zero, while the standard deviation keeps rather low and constant, compared to the energies. Then, a “turning point” is reached around $W \approx 1$, after which the standard deviation starts to increase. This is a signature of a reentrant topological phase for intermediate disorder strength, similar to the one predicted in the Kitaev model with short-range pairing [53]. In Fig. 2(c) we show the effects of the disorder when, in the clean limit, the system is in the nontrivial topological phase, with $\omega = 1$. In this case, there is a subgap state at exactly zero energy, encoded in the two unpaired Majorana modes at the endpoints of the chain [73]. Accordingly, we see that, at low enough values of W , the lowest-energy eigenvalue is pinned at zero energy, with a negligible spread of the values at a given disorder strength (witnessed by the fact that, for low W , the red plot is just a sharp line). The natural conclusion is a disorder-enforced stability of the zero-energy fermionic mode, consistently with the plot in the inset of Fig. 2(c), where we report the density of

states $\rho(\epsilon)$ at a representative value of W . The sharp, subgap peak at zero energy is the apparent counterpart of the (weak) disorder robust, subgap level at $\epsilon = 0$. At variance, at large enough values of W , the grey region overlaps with the red one: this corresponds to the disappearance of the zero-energy sharp resonance in the density of states and, ultimately, to the disappearance of the topological phase.

Figures 2(a) and 2(d) correspond to the massive topological phase. Indeed, close to the clean limit (low values of W), the red and the grey lines are well separated from each other, by an amount that, on the average, is of the order of the energy difference between the subgap state and the first bulk state over the gap. As W increases, both energies monotonically decrease, on the average, toward zero. At a critical value of W_c , which we estimate below, the two curves fuse with each other, thus signaling the disappearance of the massive topological phase, exactly like in the plot of Fig. 2(c). For $W > W_c$, both the average and the standard deviation of the energies further increase with W , similarly to what happens in Fig. 2(c). By analogy, we conclude that, in all three cases, such a behavior is a signal that the system has undergone a disorder-induced transition toward a topologically trivial phase.

To estimate W_c , we note that, at any given α and μ , on a single realization of the disorder, the chemical potential at each site lies between $\mu_- = \mu - \sqrt{3}W$ and $\mu_+ = \mu + \sqrt{3}W$. It follows that, while the average chemical potential of the disordered system, in the thermodynamic limit, is still expected to be equal to μ , increasing W increases also the probability to randomly generate finite segments of the chain ("islands") characterized by an average chemical potential μ_ℓ different from μ . Such islands are responsible for the proliferation of many low energy subgap states. Depending on μ and on the disorder strength W , the islands can be characterized by a value of μ_ℓ that belongs to a different phase compared to the clean system and can, in principle, drag the system across a topological phase transition. If we consider, for example, a clean system in the topological nontrivial phase ($\alpha > 3/2$, $|\mu| < 1$), such as the one corresponding to point C of Fig. 1(a), the formation of islands belonging to the topological trivial one ($|\mu_\ell| > 1$) will generate low energy states that can hybridize with the zero energy modes destroying them, thus driving the disordered system into the topological trivial phase. On the contrary, topological nontrivial island ($|\mu_\ell| < 1$), in a topological trivial background ($\alpha > 1$, $|\mu| > 1$), can give rise to a reentrant topological phase.

The probability of formation of such topological nontrivial (trivial) islands in a trivial (nontrivial) background depends on the number of sites having a chemical potential lying beyond the transition lines of the clean system. The same argument applies also to the topological massive case. We can define W_c as the minimum amount of disorder at which the chemical potential over some sites starts to lie outside the boundary of the origi-

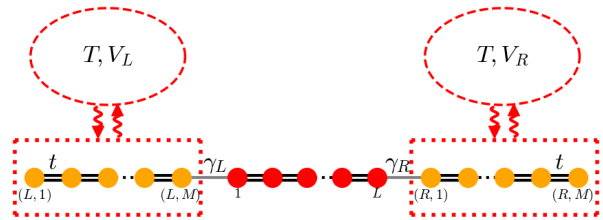


FIG. 3. Sketch of the LRK (red-dot chain) with the metallic leads (orange-dot chains) undergoing particle exchange processes (represented by the wavy red lines) with the thermal baths (reservoirs). The reservoirs (represented by the red dashed ovals) are kept at temperature T and at voltage bias (with respect to the LRK) respectively given by V_L (left reservoir) and by V_R (right reservoir).

nal phase. Eventually, we define \tilde{W}_c as the critical value at which the probability is maximum. Apparently, W_c and \tilde{W}_c depend on the two phases between which the disorder induces a transition.

To conclude this Section, we point out that, while the bulk gap provides a mean to identify the phases of the LRK in the presence of disorder, its magnitude is not an indicator of a disorder induced phase transition, as the disorder may further localize the zero-energy mode eigenfunctions, resulting in the closing of the energy gap without a phase transition in the bulk of the system [15, 53, 83]. Therefore, to exactly locate the disorder-induced transition line, one has to resort to additional methods [83], such as looking at the current \mathcal{I} and at the single-particle lead correlations $C_{L,R}$, which we do in the following of our paper.

III. LINDBLAD MASTER EQUATION APPROACH TO THE OPEN LRK MODEL

In Fig. 3, we sketch the LRK with the metallic leads, connected to the external reservoirs. We assume a thermal distribution of the fermionic modes in each reservoir and a voltage bias between the two of them, with the left (right) reservoir kept at potential V_L (V_R), with respect to the LRK. To describe the time evolution of the whole system toward the NESS, we employ the method of Refs. [50, 51, 84, 85]. In particular, assuming that the bath relaxation time is much shorter than the timescales associated to the system (LRK plus leads), we resort to Markov approximation [86, 87]. Systematically integrating over the bath degrees of freedom, we recover the Lindblad master equation (LME) approach to the open quantum system [50, 51, 71, 72, 84, 85]. In particular, to make the system evolve toward a NESS in which a finite bias is applied to the LRK via the metallic leads, we follow the approach of Ref. [84] and construct the LME so to let the reservoirs directly exchange particles with the leads. In the Markovian limit, the time evolution equation for

the density matrix $\rho(t)$ of a system described by the Hamiltonian \mathcal{H} , connected to the external leads coupled to the reservoirs, is determined by the Liouville equation, given by [71, 72]:

$$\frac{d\rho(t)}{dt} = -i[\mathcal{H}, \rho(t)] + \sum_k \left(L_k \rho(t) L_k^\dagger - \frac{1}{2} \{ L_k^\dagger L_k, \rho(t) \} \right). \quad (6)$$

In our case, \mathcal{H} in Eq. (6) coincides with the Hamiltonian governing the unitary evolution of the isolated system (LRK plus leads). The *jump operators* $\{L_k\}_k$ encode the interactions between the reservoirs and the system. To provide their explicit expressions, we model both leads (denoted, in the following, respectively with the labels L and R) as noninteracting fermionic chains at zero chemical potential, described by M -site lattice Hamiltonians for spinless fermions, $H_{(L,R)}$ given by

$$H_{(L,R)} = -t \sum_{i=1}^{M-1} \{ d_{(L,R),i}^\dagger d_{(L,R),i+1} + d_{(L,R),i+1}^\dagger d_{(L,R),i} \}, \quad (7)$$

with t being the nearest-neighbor hopping amplitude. The corresponding eigenenergies and eigenmodes, ϵ_n , $\eta_{(L,R),n}$, are given by

$$\begin{aligned} \epsilon_n &= -2t \cos(k_n) \quad (k_n = \pi n / (M+1)) \\ \eta_{(L,R),n} &= \sqrt{\frac{2}{M+1}} \sum_{j=1}^M \sin(k_n j) d_{(L,R),j}. \end{aligned} \quad (8)$$

The leads are connected to the LRK via the hopping term $H_H = H_{H,L} + H_{H,R}$, with

$$\begin{aligned} H_{H,L} &= -\gamma_L \{ d_{L,M}^\dagger \chi_1 + \chi_1^\dagger d_{L,M} \} \\ H_{H,R} &= -\gamma_R \{ d_{R,1}^\dagger \chi_L + \chi_L^\dagger d_{R,1} \}, \end{aligned} \quad (9)$$

with $\gamma_{(L,R)}$ being the hopping amplitudes. Finally, to stabilize a NESS with lead modes distributed according to Fermi distribution, we assume that the external baths interact with the metallic leads by injecting and/or extracting eigemodes, at a corresponding rate proportional to the Fermi distribution function determined by the temperature T (which we assume to be the same in all the reservoirs) and by the voltage bias [63, 64, 85]. Accordingly, we define the following set of Lindblad jump operators, respectively corresponding to the injection and to the extraction of lead excitations [84]:

$$\begin{aligned} L_{(L,R),k}^{\text{in}} &= \sqrt{2\gamma_{(L,R)} f_{(L,R)}(\epsilon_k)} \eta_{(L,R),k}^\dagger \\ L_{(L,R),k}^{\text{out}} &= \sqrt{2\gamma_{(L,R)} (1 - f_{(L,R)}(\epsilon_k))} \eta_{(L,R),k}, \end{aligned} \quad (10)$$

with the Fermi distribution function

$$f_{(L,R)}(\epsilon_k) = \frac{1}{1 + \exp\left(\frac{\epsilon_k - V_{(L,R)}}{T}\right)}, \quad (11)$$

and $V_{(L,R)}$ being the bias of the reservoir connected to the (L, R) lead. Specifically, in the following we assume $V_L = -V_R = V (> 0)$, which implies that the current flows from the left to the right, and $T = 0$.

To compute \mathcal{I} and $C_{L,R}$ we need the (time-dependent) correlation matrix elements, $\theta_{i,j}$ and $\theta_{i,j}^A$, defined as

$$\theta_{i,j}(t) = \text{Tr} \left(c_i^\dagger c_j \rho(t) \right), \quad (12)$$

$$\theta_{i,j}^A(t) = \text{Tr} \left(c_i^\dagger c_j^\dagger \rho(t) \right), \quad (13)$$

with the operators c_i given by

$$c_i = \begin{cases} d_{L,i} & \text{for } i \in [1, M] \\ \chi_{i-M} & \text{for } i \in [M+1, M+L] \\ d_{R,i-M-L} & \text{for } i \in [M+L+1, 2M+L] \end{cases}. \quad (14)$$

The diagonal elements $\theta_{i,i}(t)$ correspond to the average occupation of each site, while the off-diagonal elements are related to the normal correlation between different sites. Conversely, $\theta^A(t)$ encodes the anomalous correlations between sites. If (as it is in our case) the overall Hamiltonian is quadratic in the fermionic operators and the Lindblad jump operators are linear in the fermionic modes, it is possible to write a closed set of linear differential equations for the time evolution of the $\theta_{i,j}(t)$ and of the $\theta_{i,j}^A(t)$. To do so, we rely on the formalism presented in Appendix A, whose starting point consists in rewriting the system Hamiltonian in terms of the lattice fermion operators c_j in Eq. (14) as

$$\mathcal{H} = \sum_{i,j} \left(A_{i,j} c_i^\dagger c_j + B_{i,j} c_i^\dagger c_j^\dagger + B_{j,i}^* c_i c_j \right). \quad (15)$$

A and B in Eq. (15) are $(2M+L) \times (2M+L)$ square matrices. Writing \mathcal{H} as in Eq. (15) allows us to write in a compact form the time evolution equations for the generalized covariance matrix $\Theta(t)$, given by

$$\Theta(t) = \begin{bmatrix} \theta(t) & \theta^A(t) \\ (\theta^A(t))^\dagger & -\theta^T(t) \end{bmatrix}. \quad (16)$$

Within LME approach, the time evolution equation for $\Theta(t)$ is recovered by solving the differential equation

$$\frac{d\Theta(t)}{dt} = i[\Omega, \Theta(t)] - \frac{1}{2} \{ \Gamma + \Pi, \Theta(t) \} + \Gamma, \quad (17)$$

with the matrices Ω, Γ, Π determined by \mathcal{H} and by the Lindblad jump operators, and respectively defined as

$$\Omega = \begin{bmatrix} A^T & -2B^\dagger \\ -2B & -A \end{bmatrix}, \quad (18)$$

$$\Gamma = \begin{bmatrix} \mathcal{G} & -2iB^\dagger \\ 2iB & -\mathcal{G} \end{bmatrix}, \quad (19)$$

$$\Pi = \begin{bmatrix} \mathcal{R} & 2iB^\dagger \\ -2iB & 2\mathcal{G} + \mathcal{R} \end{bmatrix}. \quad (20)$$

We refer to Eq. (A8) of Appendix A for the rigorous definition of these matrices and for a discussion of their properties.

Equation (17) readily allows us to derive Θ at the NESS, Θ_{NESS} . Indeed, from the condition $\frac{d\Theta_{\text{NESS}}(t)}{dt} = 0$, we find

$$\mathcal{A}\Theta_{\text{NESS}} + \Theta_{\text{NESS}}\mathcal{A}^\dagger = -\Gamma, \quad (21)$$

with

$$\mathcal{A} = -\frac{1}{2}\{\Gamma + \Pi\} + i\Omega. \quad (22)$$

Equation (17), as well as the condition for recovering Θ_{NESS} , Eq. (21), are the key ingredients for our following calculation of the charge current and of the correlations.

IV. CHARGE CURRENT AND ENDPOINT CORRELATIONS BETWEEN THE LEADS IN THE NON EQUILIBRIUM STEADY STATE

Coupling the system to the reservoirs as we discuss before stabilizes a NESS in which the leads are biased at a voltage $\pm V$ with respect to the LRK. This induces a finite current \mathcal{I} through the system. In the clean limit, the behavior of \mathcal{I} as a function of V depends on whether the LRK develops subgap modes and whether they are massless, or massive. In particular, as we argue in the following within the framework of a simplified model, in which a single, massless or massive mode is coupled to the two leads, \mathcal{I} as a function of V shows an activated behavior at the energy of the mode itself. In addition, no activation is apparently expected if the system lies within the topologically trivial phase, consistently with the absence of a subgap mode in this phase. A similar behavior is shown by the single particle lead correlations across the LRK. Importantly, the activated behavior survives in the presence of disorder, though with minor modifications. This, as we show below, provides us with an effective way to probe the phase diagram of the LRK in the presence of disorder.

A. Single-level model as a reference calculation

To motivate our use of \mathcal{I} and $C_{L,R}$ to probe the phase of the LRK connected to the leads, we now preliminary analyze their behavior in a simplified model, in which the two leads are connected to a simple system made out of two real fermionic modes, with tunable overlap with each other. By extrapolation, we then generalize our conclusions to the LRK, including the effects of the disorder, as well. Following Refs. [70, 88, 89], we define the single-level lattice model Hamiltonian H_{SL} as $H_{\text{SL}} = H_{0,\text{SL}} + H_{\tau,\text{SL}} + H_\gamma$, with

$$\begin{aligned} H_{0,\text{SL}} &= -w \sum_{i=1}^{M-1} \sum_{X=L,R} \{d_{X,j}^\dagger d_{X,j+1} + d_{X,j+1}^\dagger d_{X,j}\} \\ H_\gamma &= -\frac{i}{2}\epsilon_0 \Gamma_L \Gamma_R \\ H_{\tau,\text{SL}} &= -\tau \Gamma_L (d_{L,M}^\dagger - d_{L,M}) + i\tau \Gamma_R (d_{R,1}^\dagger + d_{R,1}). \end{aligned} \quad (23)$$

In Eq. (23), $d_{(L,R),j}$ are complex lattice (lead) Dirac fermion operators, Γ_L, Γ_R are real fermionic modes, and ϵ_0 , which measures the energy splitting due to the hybridization between the Majorana modes, is our tuning parameter. To faithfully mimic the subgap behavior of the LRK, we couple the leads, described by $H_{0,\text{SM}}$, to the reservoirs, via the jump operators defined in Eqs. (10) and (11). Solving the corresponding equation for the density matrix, $\rho_{\text{SL}}(t)$, as in Eq. (6), we eventually compute both the interface current \mathcal{I}_{SL} and the (modulus of the) correlations, $|C_{L,R}|$, respectively given by

$$\begin{aligned} \mathcal{I}_{\text{SL}}(t) &= -\frac{\tau}{2} \text{Tr}[\rho_{\text{SL}}(t) \{(\Gamma_L - i\Gamma_R)d_{L,M} + \text{H.c.}\}] \\ |C_{L,R}(t)| &= |\text{Tr}[\rho_{\text{SL}}(t) d_{L,M}^\dagger d_{R,1}]|. \end{aligned} \quad (24)$$

with H.c. standing for Hermitian conjugate. As $t \rightarrow \infty$, $\mathcal{I}_{\text{SL}}(t)$ and $|C_{L,R}(t)|$ reach the value they take in the NESS, which is the quantity we plot in Figs. 4 and 5, as a function of the voltage bias V , for different, representative values of ϵ_0 (see the figure caption for details).

From the plots in Fig. 4, we note that, at a given ϵ_0 , \mathcal{I}_{SL} , as a function of V , shows an activated behavior at a threshold set at $V \sim \epsilon_0$. As we discuss above, whether the activated behavior emerges, in our system, at zero, or at a finite, bias signals whether the LRK is in the topological, or in the topological massive, phase. The same information can be recovered from the plots of $|C_{L,R}|$ as a function of V , which we show in Fig. 5. Indeed, we see that, at a given ϵ_0 , the curves show a peak, centered around $V \sim \epsilon_0$, whose location is consistent with what we get from \mathcal{I}_{SL} as a function of V in Fig. 4.

Using the results of this Section as our reference starting point, we now look at the charge current and the correlations in the NESS to study the phase of the LRK, in the clean limit as well as in the disordered case.

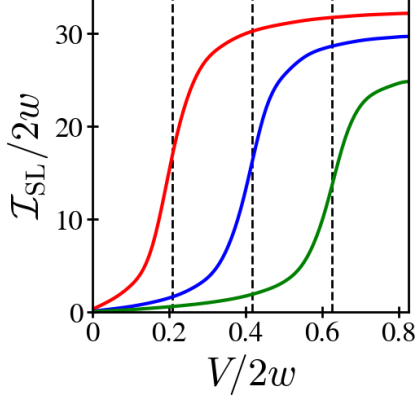


FIG. 4. Current $\mathcal{I}_{\text{SL}}/2w$ in the NESS, computed according to Eq. (24), for the system described by the Hamiltonian in Eq. (23), with the following values of the various parameters: $2w = 1$, $\tau = 0.04$, $\epsilon_0 = 0.21, 0.42, 0.63$ (red, blue and green curve, respectively). The dashed, vertical lines mark the position of the values of ϵ_0 we used in the calculations. [Note in this, and in following plots, the dimensionless quantities reported on the ordinate axis have been multiplied by 10^4 , to ease the readability of the figure.]

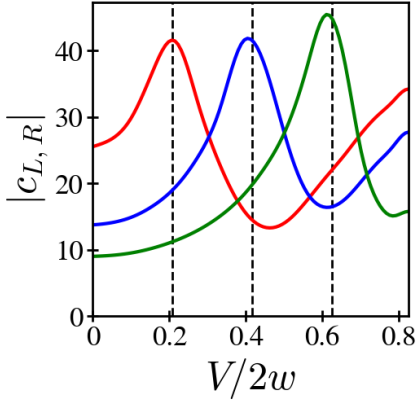


FIG. 5. $|c_{L,R}|$ in the NESS, computed according to Eq. (24), for the system described by the Hamiltonian in Eq. (23), with the following values of the various parameters: $2w = 1$, $\tau = 0.04$, $\epsilon_0 = 0.21, 0.42, 0.63$ (red, blue and green curve, respectively). The dashed, vertical lines mark the position of the values of ϵ_0 we used in the calculations.

B. Charge current through the LRK model at the NESS

Referring to the formalism of Section A and of Appendix III, we express the charge current \mathcal{I} in the normal leads by means of the continuity equation for the particle number at site j , $n_j(t) = \text{Tr}[\rho(t)c_j^\dagger c_j]$, given by

$$\begin{aligned} \frac{dn_j(t)}{dt} = & -2 \sum_{l \neq j} \Im m[A_{l,j} \theta_{l,j}(t)] \\ & - \sum_{l \neq j} \Re e[(\mathcal{G} + \mathcal{R})_{l,j}^* \theta_{l,j}(t)] + \mathcal{G}_{j,j}(1 - n_j(t)) + \mathcal{R}_{j,j} n_j(t). \end{aligned} \quad (25)$$

Eq. (25) can be readily regarded as a continuity equation, evidencing how there are two different sources of the nonzero rate of change $\frac{dn_j(t)}{dt}$. Specifically:

- The “standard” kinetic contribution, related to the nonzero hopping amplitude encoded in the matrix A . The corresponding contribution to the particle current over the link between i and j is given by [50]:

$$J_{i,j}(t) = -2 \Im m\{A_{i,j} \theta_{i,j}(t)\}. \quad (26)$$

- The second contribution, at the bottom line of Eq. (25), due to the reservoirs, that exchange particles with the leads at a given rate.

Since, in the NESS $\frac{d\Theta_{\text{NESS}}(t)}{dt} = 0$, the two contributions at the right hand side of Eq. (25) compensate with each other, so that the current $\mathcal{I} = J_{M,M+1}$ provides all the relevant information about subgap states in the LRK, just as \mathcal{I}_{SL} does in the single level, simplified model. To evidence the similar behavior of \mathcal{I} and \mathcal{I}_{SL} , in Fig. 6, we show sample plots of \mathcal{I} in the absence of disorder, along the straight lines connecting the four points ABCD in the phase diagram of Fig. 1(a).

Figure 6(a) contains plots of \mathcal{I} as a function of V , normalized to the bulk gap E_Δ , computed for $\mu = -1.25$ and $\alpha = 0.5$ (blue curve), $\alpha = 1.25$ (orange curve) and $\alpha = 2.5$ (green curve). All the three points lie over the AB segment of Fig. 1(a). At point A, which corresponds to the massive topological phase, at $V/E_\Delta \sim 0.5$, we see an activation in \mathcal{I} , which is expected to correspond to the position of the subgap massive mode. On increasing α at fixed $\mu = -1.25$, the system evolves toward point B, corresponding to the trivial phase of the LRK, with no subgap modes. The shift of the activation threshold for \mathcal{I} toward the bulk gap edge ($V/E_\Delta = 1$) witnesses that the transition from the massive topological to the trivial phase comes along with a progressive shift of the subgap mode toward the bulk gap threshold. At the same time, moving from the blue to the orange and then to the green curve, the over-all curve continuously evolves toward a plot constantly equal to 0 (for $V/E_\Delta \leq 1$), which is perfectly consistent with the expected disappearance of \mathcal{I} in the trivial phase in this range of values of V . In Fig. 6(b), we show plots drawn at constant $\alpha = 2.5$ and for $\mu = -1.25$ (blue curve), $\mu = -0.75$ (orange curve) and $\mu = 0.5$ (green curve), all lying over the BC line of Fig. 1(a), connecting point B, in the trivial phase,

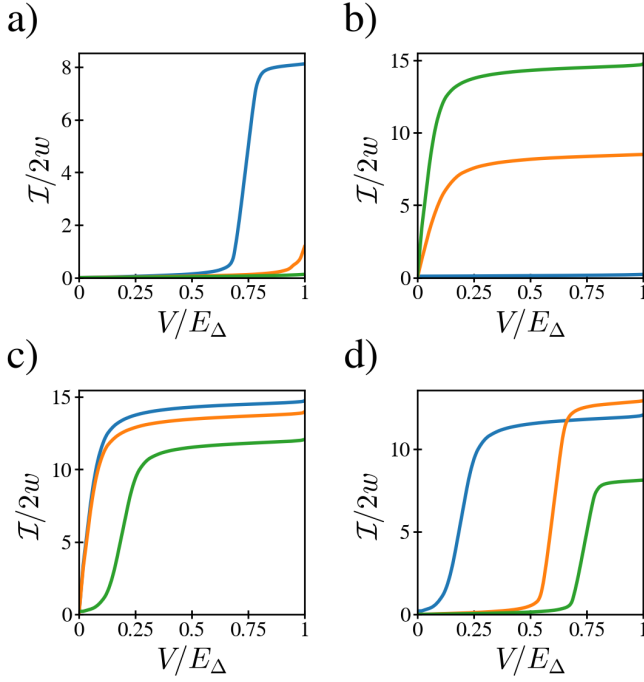


FIG. 6. Charge current $\mathcal{I}/2w$ computed, in the absence of disorder, for the LRK described by H in Eq. (1) with $2w = \Delta = 1$ and $L = 500$. The panels correspond to points over any of the four segments connecting the point A,B,C,D in the phase diagram of Fig. 1(a). In particular:

- (a): $\mu = -1.25$ for all the plots, $\alpha = 0.5$ (blue line), $\alpha = 1.25$ (orange line), $\alpha = 2.5$ (green line). These points all lie on the AB segment of Fig. 1(a);
 (b): $\alpha = 2.5$, $\mu = -1.25$ (blue line), $\mu = -0.75$ (orange line), $\mu = 0.5$ (green line). These points all lie on the BC segment of Fig. 1(a);
 (c): $\mu = 0.5$, $\alpha = 2.5$ (blue line), $\alpha = 1.25$ (orange line), $\alpha = 0.5$ (green line). These points all lie on the CD segment of Fig. 1(a);
 (d): $\alpha = 0.5$, $\mu = 0.5$ (blue line), $\mu = -0.75$ (orange line), $\mu = -1.25$ (green line). These points all lie on the DA segment of Fig. 1(a).

with point C, in the topological phase of the LRK. Tuning μ along the BC line corresponds to the “standard” topological phase transition in the Kitaev model. This means that either there are no subgap modes or, once the system has entered the topological phase, they are pinned at zero energy. At the same time, due to the resonant Andreev reflection triggered by the localized real fermionic mode at each interface [8, 90, 91], we expect a strong increase of the current across the phase transition. Indeed, Fig. 6(b) is consistent with both expectations. On one hand, on increasing μ there is an apparent increase of \mathcal{I} when entering the topological phase, at any $V/E_\Delta < 1$. On the other hand, the activation threshold keeps locked at $V/E_\Delta \sim 0$, consistently with the emergence of the localized, zero energy modes. The plots in Fig. 6(c) are drawn at $\mu = 0.5$ and with the same values of α as in Fig. 6(a), in decreasing order, starting from

$\alpha = 2.5$. Now the LRK is taken from the topological to the massive topological phase and, consistently, we see a shift of the activation threshold toward a finite value of V/E_Δ , accompanied by a mild reduction in \mathcal{I} at a given V . Finally, Fig. 6(d) summarizes the evolution of \mathcal{I} as a function of V/E_Δ when moving from point D to point A of Fig. 6(a). The shift of the activation threshold across finite values of V/E_Δ is definitely consistent with what one expects along a line connecting two massive topological phases with different values of the energy of the subgap mode.

As the above discussion evidences, the behavior of \mathcal{I} as a function of V/E_Δ for $V/E_\Delta < 1$ can be readily interpreted in terms of an effective, single level Hamiltonian as the one in Eq. (23). In the presence of disorder we compute the current going through the following, additional steps:

1. We randomly generate a configuration of the impurity potential, $\{\epsilon_i\}$, as discussed in the previous section;
2. We solve Eq. (17) for Θ_{NESS} at given $\{\epsilon_i\}$;
3. We repeat the two previous points \mathcal{N} times and eventually average over the realizations of the disorder. Accordingly, denoting with $\mathcal{I}^{(r)}$ the current computed for the r -th realization of the disorder, we compute the disorder-averaged current $\langle \mathcal{I} \rangle$ as:

$$\langle \mathcal{I} \rangle = \frac{1}{\mathcal{N}} \sum_{r=1}^{\mathcal{N}} \mathcal{I}^{(r)}. \quad (27)$$

4. Repeating the above procedure, at all the marked points A,B,C,D in Fig. 1, we construct plots of $\langle \mathcal{I} \rangle$ as a function of V/E_Δ for various values of the disorder strength W .

Remarkably, previous studies of the effects of the disorder on a topological phase have shown that, while a small amount of disorder works to enforce the topological phase(s), a strong enough value of W typically washes out the topology, typically when it becomes of the same order of magnitude as μ [47–53]. Yet, the specific interplay between disorder and topology depends on the characteristics of the reference clean phase, which, in our case, motivates our systematic analysis of the effects of increasing the disorder strength W at the points A,B,C, and D in Fig. 1.

Our main results are summarized by the plots of in Fig. 7. In particular, in Fig. 7(a), we show plots of $\langle \mathcal{I} \rangle$ vs. V/E_Δ at point A of the phase diagram of Fig. 1 at increasing values of W . While the blue curve, drawn at $W = 0.0$, shows an activated behavior at a finite value of V/E_Δ , corresponding to the location in energy of the subgap mode, on increasing W the activation threshold moves to lower (subgap) values energy. Such a behavior is qualitatively similar to the one that we show in

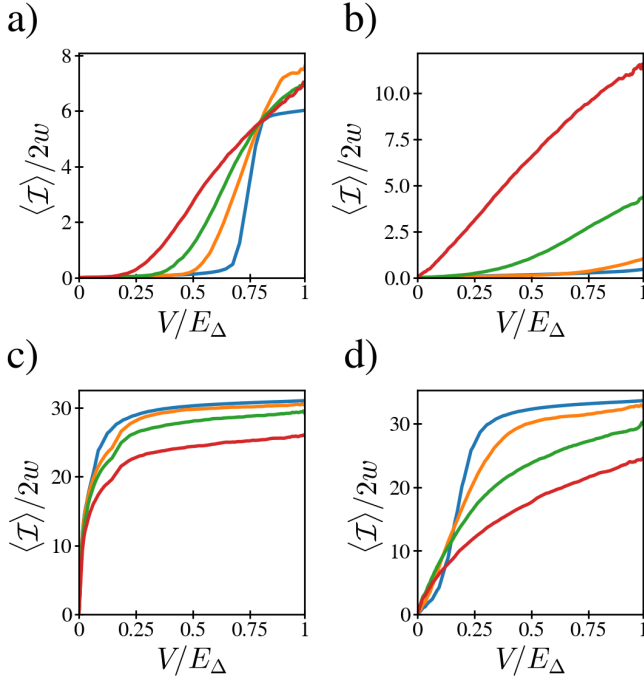


FIG. 7. $\langle \mathcal{I} \rangle / 2w$ computed at the NESS for the LRK with $2w = \Delta = 1$, $L = 100$, connected to metallic leads with $M = 101$ and variable single electron hopping strengths $\gamma_R = \gamma_L = 0.05$. The coupling strengths between the leads and the reservoirs are set at $g = 0.01$. In any case, the temperature is set to 0. The strength of the disorder is varied as detailed in the following. $\langle \mathcal{I} \rangle / 2w$ vs V/E_Δ at points (a) A, (b) B, (c) C, and (d) D of Fig. 1 for disorder $W = 0$ (blue curve), $W = 0.2$ (orange curve), $W = 0.4$ (green curve), $W = 0.6$ (red curve).

Fig. 7(d), corresponding to point D, which is in the same (massive topological) phase as point A, although, due to the relatively smaller value of the subgap mode energy, the shift in the activation threshold is not as evident as at point A. Conversely, Figs. 7(b) and 7(c) are consistent with the known results for the short-range pairing, disordered Kitaev model [52, 53]. Specifically, the persistence, at increasing W , of the activation threshold at $V/E_\Delta = 0$ in Fig. 7(c) evidences that a limited amount of disorder does not affect the topological phase and only results in a relatively small lowering of $\langle \mathcal{I} \rangle$ on increasing the disorder strength, while the absence of a well-defined threshold in Fig. 7(b) corresponds to the absence of subgap modes in the clean limit, with the increase of $\langle \mathcal{I} \rangle$ on increasing W possibly determined by the proliferation of disorder-induced subgap states.

The shift toward zero energy, at increasing disorder, of the activation threshold in Figs. 7(a) and 7(d) evidences how a limited amount of disorder enforces the localization of edge modes in the short-range Kitaev model. Consistently, the finite energy subgap mode in the massive topological phase of the LRK can be thought of as due to the long-range hybridization between edge modes [27]. Indeed, an increase in the localization of the bound-

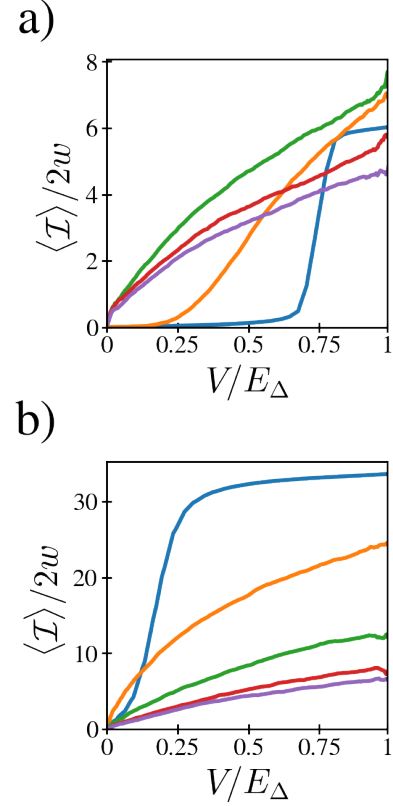


FIG. 8. $\langle \mathcal{I} \rangle / 2w$ computed for the same system as in Fig. 7(a) (panel (a)) and in Fig. 7(d) (panel (b)), with $W = 0$ (blue curve), $W = 0.6$ (orange curve), $W = 1.2$ (green curve), $W = 1.8$ (red curve), $W = 2.0$ (purple curve).

ary modes corresponds to a decrease in the corresponding energy, which is perfectly consistent with the shift in the activation threshold toward lower energy on increasing W . This suggests the possibility of realizing a disorder induced phase transition from the massive topological phase to the short-range topological phase which, in the clean limit, would only be possible upon tuning an hardly tunable parameter, such as α .

To further ground our conclusions, in Fig. 8 we plot $\langle \mathcal{I} \rangle$ versus V/E_Δ at points A and D, up to values of the disorder strength as large as $W = 2.0$. In Fig. 8(a), we note the shift of the activation threshold to zero energy and the rise of $\langle \mathcal{I} \rangle$ with W at a given value of V/E_Δ . This is consistent with a transition toward the (short-range) topological phase, roughly at W between 1.0 and 1.2. The subsequent decrease of the current for larger values of W is, instead, consistent with the effects of adding disorder to the system in the topological phase. At variance, the monotonical decrease of $\langle \mathcal{I} \rangle$ with increasing W in Fig. 8(b) is consistent with either a direct transition toward the trivial phase, or with no transitions at all.

To double check the conclusions of this section, in the following, we perform a similar study of the behavior of the endpoint correlations across the LRK.

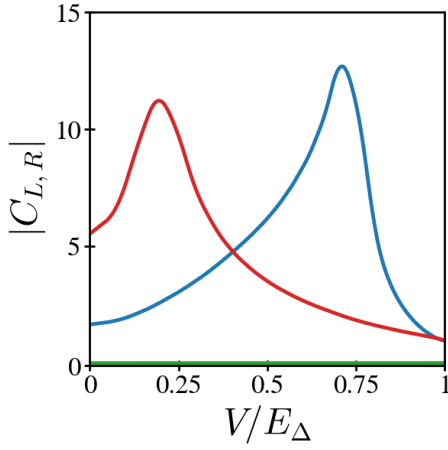


FIG. 9. $|C_{L,R}|$ computed for the same system as in Fig. 6, at points A (blue curve), B (orange curve), C (green curve), and D (red curve) of Fig. 1(a). Note that the orange and the green curve have collapsed onto the $|C_{L,R}| = 0$ axis.

C. Endpoint correlations between the leads

In the absence of disorder, the correlation $C_{L,R}$ is expressed in terms of the covariance matrix elements as

$$C_{L,R} = \theta_{M,M+L+1} . \quad (28)$$

Introducing disorder, Eq. (28) is generalized by averaging over a number \mathcal{N} of independent disorder realizations, that is

$$C_{L,R} = \frac{1}{\mathcal{N}} \sum_{r=1}^{\mathcal{N}} \theta_{M,M+L+1}^{(r)} . \quad (29)$$

In Fig. 9, we show our result for $|C_{L,R}|$, as a function of V/E_{Δ} , in the absence of disorder and for $V/E_{\Delta} < 1$, at the four points A, B, C, and D in Fig. 1(a). While, at the A and D points, $|C_{L,R}|$ shows a peak centered at an energy consistent with the position of the activation threshold of \mathcal{I} in the clean limit (blue and red curve, respectively), the curves corresponding to points B and C, within the whole interval $0 \leq V/E_{\Delta} < 1$, keep smaller than the previous ones by several order of magnitudes: they are basically constantly equal to 0. As expected from our previous discussion of the simplified model, this is consistent with either the absence of subgap modes (point B), or with the lack of hybridization between the real fermionic modes (point C).

In the disordered case, since disorder typically favors the localization, we expect no relevant effects at points B and C. For this reason, in the following we focus on points A and D of the phase diagram. In Fig. 10, we plot $|C_{L,R}|$ as a function of V/E_{Δ} , computed at points A and D of the phase diagram, at increasing disorder strength W (see figure caption for details).

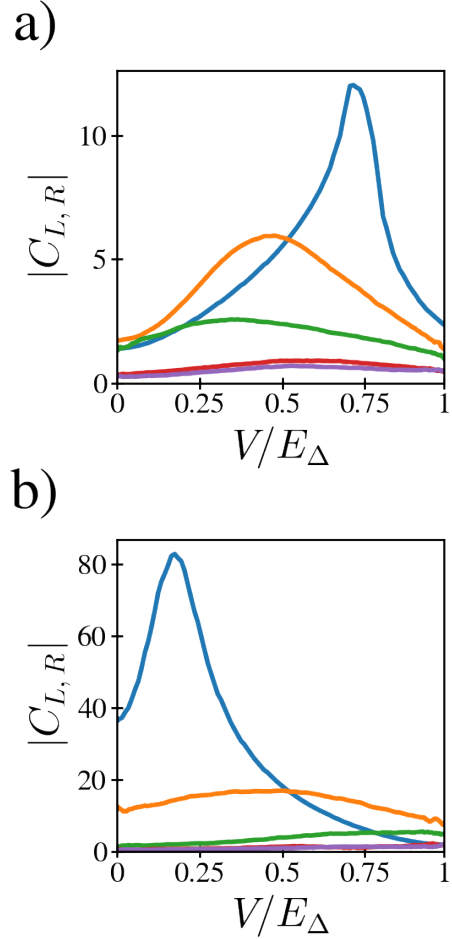


FIG. 10. $|C_{L,R}|$ computed for the same system as in Fig. 8, at points A (panel (a)) and D (panel (b)) of the phase diagram of the LRK, with $W = 0.0$ (blue curve), $W = 0.6$ (orange curve), $W = 1.2$ (green curve), $W = 1.8$ (red curve), $W = 2.0$ (purple curve).

Specifically, Fig. 10(a) corresponds to point A of the phase diagram, Fig. 10(b) to point D. We note that, while, in both cases, there is a strong suppression of $|C_{L,R}|$ on increasing W , in Fig. 10(a) there is no inversion of the main trend, such as in Fig. 8(a), at large disorder strength. In fact, as we remark above, the correlations do not allow to resolve the trivial from the short-range topological phase. Yet, combining the plots of Fig. 10 with the ones on Fig. 8, provides a comprehensive picture of what are the effects of the disorder in the various phases of the LRK, suggesting, in addition, the intriguing possibility that the disorder itself might trigger a direct transition from the massive to the short-range topological and, eventually, to the trivial phase.

V. CONCLUDING REMARKS

We have made a combined study of the phase diagram of the disordered LRK, connected to thermal reservoirs by means of metallic leads, by first monitoring the lowest and the second lowest energy eigenvalue of the LRK Hamiltonian at increasing disorder strength, then, by computing the current flowing through the interfaces between the LRK and the leads at a finite bias between the reservoirs and, finally, by looking at the endpoint correlations across the LRK.

Our method has allowed us to circumvent the difficulty of defining a topological invariant, such as the Chern number, in the disordered system. Apart from mapping out the various phases of the disordered system, we have evidenced how a limited amount of disorder (small W) induces reentrant massive topological phases in the LRK (points B and C of the phase diagram in Fig. 1) that are analogous to the disorder induced reentrant topological phase of the Kitaev model. In particular, while a limited amount of disorder makes the system behave similarly to what expected in the short-range topological phase, a strong disorder washes out the topological phase, just as in the short-range case. Again there is a reentrant behavior in the phase diagram, as disorder is increased, but this time toward a different topological phase.

Aside from providing a first, comprehensive study of the disordered LRK, the results we obtained within our approach call for an extension of our work to make, for instance, a sharp verification of whether it is possible to recover a direct transition between the massive and the short-range topological phase by acting on the disorder only, possibly changing the functional form of the disorder potential as, for instance, done in Refs. [50, 51]. Yet, this, as well as other possible developments of our results, go beyond the scope of this work and will possibly be analyzed in forthcoming research projects. The data that support the findings of this article are openly available at [92]

ACKNOWLEDGMENTS

A. N. acknowledges funding by the Deutsche Forschungsgemeinschaft (DFG, German Research Foundation), Projektnummer 277101999 – TRR 183 (project C01), under project No. EG 96/13-1, and under Germany's Excellence Strategy – Cluster of Excellence Matter and Light for Quantum Computing (ML4Q) EXC 2004/1 – 390534769. E.G.C. acknowledges funding (partially) supported by ICSC Centro Nazionale di Ricerca in High Performance Computing, Big Data and Quantum Computing, funded by European Union—NextGenerationEU.

Appendix A: Lindblad Master Equation for the correlation matrix

In this Appendix we present the main mathematical steps behind the formalism of Sec. III. In the following, we consider a generic quadratic fermion Hamiltonian \mathcal{H} , containing single-fermion pairing and hopping terms, in the form

$$\mathcal{H} = \sum_{i,j} \left(A_{i,j} c_i^\dagger c_j + B_{i,j} c_i^\dagger c_j^\dagger + B_{j,i}^* c_i c_j \right), \quad (\text{A1})$$

with c_i, c_j^\dagger being lattice fermionic operators satisfying the anticommutation algebra $\{c_i, c_j^\dagger\} = \delta_{i,j}$ (all the other anticommutators being equal to 0), $A^\dagger = A$ and $B^T = -B$. Starting from Eq. (6) for the density matrix $\rho(t)$ and defining the Lindblad jump operators as in Eq. (11), we readily obtain the time evolution equation for $\theta_{i,j} = \langle c_i^\dagger c_j \rangle$, with $\langle \dots \rangle = \text{Tr}[\rho(t) \dots]$, in the form

$$\begin{aligned} \frac{d\theta_{i,j}(t)}{dt} = & -i \left\langle \left[c_i^\dagger c_j, \mathcal{H} \right] \right\rangle \\ & + \sum_{n=(L,R),k} \left(\left\langle (L_{n,k}^{\text{in}})^\dagger c_i^\dagger c_j L_{n,k}^{\text{in}} \right\rangle - \frac{1}{2} \left\langle \left\{ c_i^\dagger c_j, (L_{n,k}^{\text{in}})^\dagger L_{n,k}^{\text{in}} \right\} \right\rangle \right) \\ & + \sum_{n=(L,R),k} \left(\left\langle (L_{n,k}^{\text{out}})^\dagger c_i^\dagger c_j L_{n,k}^{\text{out}} \right\rangle - \frac{1}{2} \left\langle \left\{ c_i^\dagger c_j, (L_{n,k}^{\text{out}})^\dagger L_{n,k}^{\text{out}} \right\} \right\rangle \right). \end{aligned} \quad (\text{A2})$$

Note that, in writing Eq. (A2), we refer to a specific system such as the one we introduce and discuss in Sec. IV, that is, a central region consisting of a one-dimensional, L -site lattice, with two, one-dimensional, M -site, metallic leads, attached to the endpoints of the chain. To recover the explicit form of the right-hand side of Eq. (A2), we employ the following chain of identities (that are readily recovered from the cyclic property of the trace):

$$\begin{aligned} & \sum_{l,m} \left\langle \left[c_i^\dagger c_j, A_{l,m} c_l^\dagger c_m + B_{l,m} c_l^\dagger c_m^\dagger + B_{l,m}^* c_m c_l \right] \right\rangle \\ & = \sum_{l,m} \left\{ A_{l,m} \left\langle \left[c_i^\dagger c_j, c_l^\dagger c_m \right] \right\rangle \right. \\ & \quad + B_{l,m} \left\langle \left[c_i^\dagger c_j, c_l^\dagger c_m^\dagger \right] \right\rangle \\ & \quad \left. + B_{l,m}^* \left\langle \left[c_i^\dagger c_j, c_m c_l \right] \right\rangle \right\} \\ & = \sum_{l,m} \left[A_{l,m} \left(\delta_{j,l} \left\langle c_i^\dagger c_m \right\rangle - \delta_{i,m} \left\langle c_l^\dagger c_j \right\rangle \right) \right. \\ & \quad + B_{l,m} \left(\delta_{j,l} \left\langle c_i^\dagger c_m^\dagger \right\rangle - \delta_{j,m} \left\langle c_l^\dagger c_i^\dagger \right\rangle \right) \\ & \quad \left. + B_{l,m}^* \left(\delta_{i,m} \left\langle c_l c_j \right\rangle - \delta_{i,l} \left\langle c_m c_j \right\rangle \right) \right] \\ & = - \left\{ [A^T, \theta(t)] + 2i (\theta^A(t) B + B^* (\theta^A(t))^+) \right\}_{ij}, \end{aligned} \quad (\text{A3})$$

with $\theta(t)$ and $\theta^A(t)$ being the matrices with elements respectively given by $\theta_{i,j}(t)$ and by $\theta_{i,j}^A(t)$. To pertinently

rewrite the Liouvillian term, denoting with $d_{(L,R),j}$ the real space, single fermion operators for the leads, we obtain

$$L_{(L,R),k}^{\text{in}} = \sqrt{2\gamma f(\epsilon_k)} \sum_{j=1}^M S_{k,j}^* d_{(L,R),j}^\dagger ,$$

$$L_{(L,R),k}^{\text{out}} = \sqrt{2\gamma(1-f(\epsilon_k))} \sum_{j=1}^M S_{k,j} d_{(L,R),j} , \quad (\text{A4})$$

with the d -operators defined as in Eq. (14), and

$$S_{j,k} = \sqrt{\frac{2}{M+1}} \sin(kj) . \quad (\text{A5})$$

Using Eqs. (A4) and (A5), we eventually obtain

$$\begin{aligned} & \sum_{n=(L,R),k} \left(\langle (L_{n,k}^{\text{in}})^\dagger c_i^\dagger c_j L_{n,k}^{\text{in}} \rangle - \frac{1}{2} \langle \{ c_i^\dagger c_j, (L_{n,k}^{\text{in}})^\dagger L_{n,k}^{\text{in}} \} \rangle \right) \text{by} \\ & \sum_{n=(L,R),k} \left(\langle (L_{n,k}^{\text{out}})^\dagger c_i^\dagger c_j L_{n,k}^{\text{out}} \rangle - \frac{1}{2} \langle \{ c_i^\dagger c_j, (L_{n,k}^{\text{out}})^\dagger L_{n,k}^{\text{out}} \} \rangle \right) \frac{d\theta^A(t)}{dt} = i(\theta^A(t)A + A^T\theta^A(t)) - 2i(B^*\theta^T(t) + \theta B^*) \\ & 2\gamma \sum_{n=(L,R)} \sum_{k,i,m} S_{l,k} S_{m,k} f(\epsilon_k) \times \\ & \left(\langle d_{n,l} c_i^\dagger c_j d_{n,m}^\dagger \rangle - \frac{1}{2} \langle \{ c_i^\dagger c_j, d_{n,l} d_{n,m}^\dagger \} \rangle \right) \\ & + 2\gamma \sum_{n=(L,R)} \sum_{k,i,m} S_{l,k} S_{m,k} (1-f(\epsilon_k)) \times \\ & \left(\langle d_{n,l}^\dagger c_i^\dagger c_j d_{n,m} \rangle - \frac{1}{2} \langle \{ c_i^\dagger c_j, d_{n,l}^\dagger d_{n,m} \} \rangle \right) . \end{aligned} \quad (\text{A6})$$

As a next step, we now introduce the matrices G_N, R_N , whose elements are given by

$$(G_N)_{l,m} = 2\gamma \sum_k S_{l,k} S_{m,k} f(\epsilon_k) ,$$

$$(R_N)_{l,m} = 2\gamma \sum_k S_{l,k} S_{m,k} [1-f(\epsilon_k)] . \quad (\text{A7})$$

Using the matrices in Eqs.(A7), we can eventually write the time evolution equation for $\theta(t)$ in a compact form,

in terms of the matrices \mathcal{G}, \mathcal{R} . These are defined as $(L+2M) \times (L+2M)$ square matrices and, in a block representation, they are given by

$$\mathcal{G}(\mathcal{R}) = \begin{bmatrix} G_N(R_N) & \mathbf{0} & \mathbf{0} \\ \mathbf{0} & \mathbf{0} & \mathbf{0} \\ \mathbf{0} & \mathbf{0} & G_N(R_N) \end{bmatrix} . \quad (\text{A8})$$

In terms of \mathcal{G} and of \mathcal{R} , as well as of the matrices A and B introduced in Eq. (A1), we obtain the time evolution equation for $\theta(t)$ in the form:

$$\begin{aligned} \frac{d\theta(t)}{dt} &= i[A^T, \theta(t)] + 2i(\theta^A(t)B + B^*(\theta^A(t))^\dagger) \\ &- \frac{1}{2}\{\mathcal{G} + \mathcal{R}, \theta(t)\} + \mathcal{G} . \end{aligned} \quad (\text{A9})$$

Going through perfectly analogous steps, we recover the time evolution equation for $\theta^A(t)$, as well. This is given

$$- \frac{1}{2}\{\mathcal{G} + \mathcal{R}, \theta^A(t)\} + 2iB^* . \quad (\text{A10})$$

Combining together Eqs.(A9) and (A10), we obtain the time evolution equation for the matrix $\Theta(t)$ defined in the main text, taking into account that, in the case of the LRK connected to metallic leads, A and B take the form

$$A = \begin{bmatrix} A_{N_L} & A_{N_L,LRK}^{\text{hop}} & \mathbf{0} \\ A_{N_L,LRK}^{\text{hop}} & A_{LRK} & A_{LRK,N_R}^{\text{hop}} \\ \mathbf{0} & A_{LRK,N_R}^{\text{hop}} & A_{N_R} \end{bmatrix}$$

$$B = \begin{bmatrix} \mathbf{0} & \mathbf{0} & \mathbf{0} \\ \mathbf{0} & B_{LRK} & \mathbf{0} \\ \mathbf{0} & \mathbf{0} & \mathbf{0} \end{bmatrix} , \quad (\text{A11})$$

with A_{N_L}, A_{N_R} being $M \times M$ matrices, $A_{N_L,LRK}^{\text{hop}}, A_{LRK,N_R}^{\text{hop}}$ ($A_{LRK,N_L}^{\text{hop}}, A_{N_R,LRK}^{\text{hop}}$) being $M \times L$ ($L \times M$) matrices, and A_{LRK}, B_{LRK} being $L \times L$ matrices.

-
- [1] M. Z. Hasan and C. L. Kane, Colloquium: Topological insulators, Rev. Mod. Phys. **82**, 3045 (2010).
[2] X.-L. Qi and S.-C. Zhang, Topological insulators and superconductors, Rev. Mod. Phys. **83**, 1057 (2011).
[3] G. Moore and N. Read, Nonabelions in the fractional quantum Hall effect, Nuclear Physics B **360**, 362 (1991).
[4] C. Nayak, S. H. Simon, A. Stern, M. Freedman, and S. Das Sarma, Non-abelian anyons and topological quan-

- tum computation, Rev. Mod. Phys. **80**, 1083 (2008).
[5] Y. Oreg, G. Refael, and F. von Oppen, Helical liquids and Majorana bound states in quantum wires, Phys. Rev. Lett. **105**, 177002 (2010).
[6] S. H. Mousavi, A. B. Khanikaev, and Z. Wang, Topologically protected elastic waves in phononic metamaterials, Nature Communications **6**, 8682 (2015).

- [7] M. V. Berry, Quantal phase factors accompanying adiabatic changes, *Proceedings of the Royal Society of London. A. Mathematical and Physical Sciences* **392**, 45 (1984).
- [8] L. Fidkowski, T. S. Jackson, and I. Klich, Model characterization of gapless edge modes of topological insulators using intermediate Brillouin-zone functions, *Phys. Rev. Lett.* **107**, 036601 (2011).
- [9] B.-H. Chen and D.-W. Chiou, An elementary rigorous proof of bulk-boundary correspondence in the generalized Su-Schrieffer-Heeger model, *Physics Letters A* **384**, 126168 (2020).
- [10] W.-H. Zhong, W.-L. Li, Y.-C. Chen, and X.-J. Yu, Topological edge modes and phase transitions in a critical fermionic chain with long-range interactions, *Phys. Rev. A* **110**, 022212 (2024).
- [11] L. Li, Z. Xu, and S. Chen, Topological phases of generalized Su-Schrieffer-Heeger models, *Phys. Rev. B* **89**, 085111 (2014).
- [12] C. Li and A. E. Miroshnichenko, Extended ssh model: Non-local couplings and non-monotonous edge states, *Physics* **1**, 2 (2019).
- [13] R. K. Malakar and A. K. Ghosh, Engineering topological phases of any winding and chern numbers in extended Su-Schrieffer-Heeger models, *Journal of Physics: Condensed Matter* **35**, 335401 (2023).
- [14] B. Pérez-González, M. Bello, A. Gómez-León, and G. Platero, Interplay between long-range hopping and disorder in topological systems, *Phys. Rev. B* **99**, 035146 (2019).
- [15] X.-S. Li, J.-R. Li, S.-F. Zhang, L.-L. Zhang, and W.-J. Gong, Topological properties of the dimerized Kitaev chain with long-range couplings, *Results in Physics* **30**, 104837 (2021).
- [16] Y. Niu, S. B. Chung, C.-H. Hsu, I. Mandal, S. Raghu, and S. Chakravarty, Majorana zero modes in a quantum Ising chain with longer-ranged interactions, *Phys. Rev. B* **85**, 035110 (2012).
- [17] W. DeGottardi, M. Thakurathi, S. Vishveshwara, and D. Sen, Majorana fermions in superconducting wires: Effects of long-range hopping, broken time-reversal symmetry, and potential landscapes, *Phys. Rev. B* **88**, 165111 (2013).
- [18] S. Lieu, D. K. K. Lee, and J. Knolle, Disorder protected and induced local zero-modes in longer-range Kitaev chains, *Phys. Rev. B* **98**, 134507 (2018).
- [19] F. Cardano, A. D'Errico, A. Dauphin, M. Maffei, B. Piccirillo, C. de Lisio, G. De Filippis, V. Cataudella, E. Santamato, L. Marrucci, M. Lewenstein, and P. Massignan, Detection of Zak phases and topological invariants in a chiral quantum walk of twisted photons, *Nature Communications* **8**, 15516 (2017).
- [20] A. D'Errico, F. Di Colandrea, R. Barboza, A. Dauphin, M. Lewenstein, P. Massignan, L. Marrucci, and F. Cardano, Bulk detection of time-dependent topological transitions in quenched chiral models, *Phys. Rev. Res.* **2**, 023119 (2020).
- [21] P. Schauß, M. Cheneau, M. Endres, T. Fukuhara, S. Hild, A. Omran, T. Pohl, C. Gross, S. Kuhr, and I. Bloch, Observation of spatially ordered structures in a two-dimensional Rydberg gas, *Nature* **491**, 87 (2012).
- [22] S. K. Kanungo, J. D. Whalen, Y. Lu, M. Yuan, S. Dasgupta, F. B. Dunning, K. R. A. Hazzard, and T. C. Killian, Realizing topological edge states with Rydberg-atom synthetic dimensions, *Nature Communications* **13**, 972 (2022).
- [23] E. J. Meier, F. A. An, A. Dauphin, M. Maffei, P. Massignan, T. L. Hughes, and B. Gadway, Observation of the topological Anderson insulator in disordered atomic wires, *Science* **362**, 929 (2018), <https://www.science.org/doi/pdf/10.1126/science.aat3406>.
- [24] D.-W. Wang, C.-S. Zhao, S.-L. Chao, R. Peng, J. Yang, Z. Yang, and L. Zhou, Simulating topological phases with atom arrays in an optical waveguide, *Opt. Express* **30**, 42347 (2022).
- [25] J. Kang, R. Wei, Q. Zhang, and G. Dong, Topological photonic states in waveguide arrays, *Advanced Physics Research* **2**, 2200053 (2023), <https://onlinelibrary.wiley.com/doi/pdf/10.1002/apxr.202200053>.
- [26] F. Grusdt, M. Hönig, and M. Fleischhauer, Topological edge states in the one-dimensional superlattice Bose-Hubbard model, *Phys. Rev. Lett.* **110**, 260405 (2013).
- [27] D. Vodola, L. Lepori, E. Ercolessi, and G. Pupillo, Long-range Ising and Kitaev models: phases, correlations and edge modes, *New Journal of Physics* **18**, 015001 (2015).
- [28] A. Alecce and L. Dell'Anna, Extended Kitaev chain with longer-range hopping and pairing, *Phys. Rev. B* **95**, 195160 (2017).
- [29] K. Patrick, T. Neupert, and J. K. Pachos, Topological quantum liquids with long-range couplings, *Phys. Rev. Lett.* **118**, 267002 (2017).
- [30] F. Pientka, L. I. Glazman, and F. von Oppen, Topological superconducting phase in helical Shiba chains, *Phys. Rev. B* **88**, 155420 (2013).
- [31] F. Pientka, L. I. Glazman, and F. von Oppen, Unconventional topological phase transitions in helical Shiba chains, *Phys. Rev. B* **89**, 180505 (2014).
- [32] T. Graß and M. Lewenstein, Trapped-ion quantum simulation of tunable-range heisenberg chains, *EPJ Quantum Technology* **1**, 8 (2014).
- [33] P. Hauke and L. Tagliacozzo, Spread of correlations in long-range interacting quantum systems, *Phys. Rev. Lett.* **111**, 207202 (2013).
- [34] A. Dutta and A. Dutta, Probing the role of long-range interactions in the dynamics of a long-range Kitaev chain, *Phys. Rev. B* **96**, 125113 (2017).
- [35] L. Cevolani, J. Despres, G. Carleo, L. Tagliacozzo, and L. Sanchez-Palencia, Universal scaling laws for correlation spreading in quantum systems with short- and long-range interactions, *Phys. Rev. B* **98**, 024302 (2018).
- [36] S. Nandy, K. Sengupta, and A. Sen, Periodically driven integrable systems with long-range pair potentials, *Journal of Physics A: Mathematical and Theoretical* **51**, 334002 (2018).
- [37] U. Bhattacharya, S. Maity, A. Dutta, and D. Sen, Critical phase boundaries of static and periodically kicked long-range Kitaev chain, *Journal of Physics: Condensed Matter* **31**, 174003 (2019).
- [38] T. Koffel, M. Lewenstein, and L. Tagliacozzo, Entanglement entropy for the long-range Ising chain in a transverse field, *Phys. Rev. Lett.* **109**, 267203 (2012).
- [39] L. Pezzè, M. Gabbriellini, L. Lepori, and A. Smerzi, Multipartite entanglement in topological quantum phases, *Phys. Rev. Lett.* **119**, 250401 (2017).
- [40] N. A. Olekhno, A. D. Rozenblit, V. I. Kachin, A. A. Dmitriev, O. I. Burmistrov, P. S. Seregin, D. V. Zhirihin, and M. A. Gorlach, Higher-order topological states mediated by long-range coupling in d_4 -symmetric lattices

- (2021), arXiv:2103.08980 [cond-mat.mes-hall].
- [41] G. Kim, J. Suh, D. Lee, N. Park, and S. Yu, Long-range-interacting topological photonic lattices breaking channel-bandwidth limit, *Light: Science & Applications* **13**, 189 (2024).
 - [42] Z.-X. Gong, M. F. Maghrebi, A. Hu, M. L. Wall, M. Foss-Feig, and A. V. Gorshkov, Topological phases with long-range interactions, *Phys. Rev. B* **93**, 041102 (2016).
 - [43] J. A. Medina-Vázquez, Influence of asymmetric long-range interactions on corner states in photonic higher-order topological insulators, *Phys. Rev. A* **107**, 043503 (2023).
 - [44] P. W. Anderson, Absence of diffusion in certain random lattices, *Phys. Rev.* **109**, 1492 (1958).
 - [45] E. Abrahams, P. W. Anderson, D. C. Licciardello, and T. V. Ramakrishnan, Scaling theory of localization: Absence of quantum diffusion in two dimensions, *Phys. Rev. Lett.* **42**, 673 (1979).
 - [46] F. Evers and A. D. Mirlin, Anderson transitions, *Rev. Mod. Phys.* **80**, 1355 (2008).
 - [47] Z.-W. Zuo and D. Kang, Reentrant localization transition in the Su-Schrieffer-Heeger model with random-dimer disorder, *Phys. Rev. A* **106**, 013305 (2022).
 - [48] J. Li, R.-L. Chu, J. K. Jain, and S.-Q. Shen, Topological anderson insulator, *Phys. Rev. Lett.* **102**, 136806 (2009).
 - [49] S.-N. Liu, G.-Q. Zhang, L.-Z. Tang, and D.-W. Zhang, Topological Anderson insulators induced by random binary disorders, *Physics Letters A* **431**, 128004 (2022).
 - [50] A. Nava, G. Campagnano, P. Sodano, and D. Giuliano, Lindblad master equation approach to the topological phase transition in the disordered Su-Schrieffer-Heeger model, *Phys. Rev. B* **107**, 035113 (2023).
 - [51] E. G. Cinnirella, A. Nava, G. Campagnano, and D. Giuliano, Fate of high winding number topological phases in the disordered extended Su-Schrieffer-Heeger model, *Phys. Rev. B* **109**, 035114 (2024).
 - [52] F. Pientka, A. Romito, M. Duckheim, Y. Oreg, and F. von Oppen, Signatures of topological phase transitions in mesoscopic superconducting rings, *New Journal of Physics* **15**, 025001 (2013).
 - [53] A. Nava, R. Giuliano, G. Campagnano, and D. Giuliano, Persistent current and zero-energy Majorana modes in a p -wave disordered superconducting ring, *Phys. Rev. B* **95**, 155449 (2017).
 - [54] X. Cai, Disordered Kitaev chains with long-range pairing, *Journal of Physics: Condensed Matter* **29**, 115401 (2017).
 - [55] J. Fraxanet, U. Bhattacharya, T. Grass, D. Rakshit, M. Lewenstein, and A. Dauphin, Topological properties of the long-range Kitaev chain with Aubry-André-Harper modulation, *Phys. Rev. Res.* **3**, 013148 (2021).
 - [56] U. Mishra, R. Jafari, and A. Akbari, *Journal of Physics A: Mathematical and Theoretical* **53**, 375301 (2020).
 - [57] R. Baghran, R. Jafari, and A. Langari, Competition of long-range interactions and noise at a ramped quench dynamical quantum phase transition: The case of the long-range pairing Kitaev chain, *Phys. Rev. B* **110**, 064302 (2024).
 - [58] Q. Niu and D. J. Thouless, Quantised adiabatic charge transport in the presence of substrate disorder and many-body interaction, *Journal of Physics A: Mathematical and General* **17**, 2453 (1984).
 - [59] Z. Fedorova, H. Qiu, S. Linden, and J. Kroha, Observation of topological transport quantization by dissipation in fast thouless pumps, *Nature Communications* **11**, 3758 (2020).
 - [60] I. Mondragon-Shem, T. L. Hughes, J. Song, and E. Prodan, Topological criticality in the chiral-symmetric aiii class at strong disorder, *Phys. Rev. Lett.* **113**, 046802 (2014).
 - [61] L. Lin, Y. Ke, and C. Lee, Real-space representation of the winding number for a one-dimensional chiral-symmetric topological insulator, *Phys. Rev. B* **103**, 224208 (2021).
 - [62] F. Hamano and T. Fukui, Flow of unitary matrices: Real-space winding numbers in one and three dimensions, *Phys. Rev. B* **110**, 045437 (2024).
 - [63] A. Nava, C. A. Perroni, R. Egger, L. Lepori, and D. Giuliano, Dissipation-driven dynamical topological phase transitions in two-dimensional superconductors, *Phys. Rev. B* **109**, L041107 (2024).
 - [64] A. Nava, C. A. Perroni, R. Egger, L. Lepori, and D. Giuliano, Lindblad master equation approach to the dissipative quench dynamics of planar superconductors, *Phys. Rev. B* **108**, 245129 (2023).
 - [65] Z. Lu and O. Raz, Nonequilibrium thermodynamics of the Markovian Mpemba effect and its inverse, *Proceedings of the National Academy of Sciences* **114**, 5083 (2017).
 - [66] A. Nava and R. Egger, Mpemba effects in open nonequilibrium quantum systems, *Phys. Rev. Lett.* **133**, 136302 (2024).
 - [67] N. Ackermann, A. Zazunov, S. Park, R. Egger, and A. L. Yeyati, Dynamical parity selection in superconducting weak links, *Phys. Rev. B* **107**, 214515 (2023).
 - [68] K. Zatsarynna, A. Nava, A. Zazunov, and R. Egger, Many-body quantum dynamics of spin-orbit coupled andreev states in a zeeman field, *Phys. Rev. B* **109**, 214505 (2024).
 - [69] A. Nava and M. Fabrizio, Dissipative cooling induced by pulse perturbations, *SciPost Phys.* **12**, 14 (2022).
 - [70] D. Giuliano, S. Paganelli, and L. Lepori, Current transport properties and phase diagram of a Kitaev chain with long-range pairing, *Phys. Rev. B* **97**, 155113 (2018).
 - [71] G. Lindblad, On the generators of quantum dynamical semigroups, *Communications in Mathematical Physics* **48**, 119 (1976).
 - [72] P. Pearle, Simple derivation of the Lindblad equation, *European Journal of Physics* **33**, 805 (2012).
 - [73] A. Y. Kitaev, Unpaired Majorana fermions in quantum wires, *Physics-Uspekhi* **44**, 131 (2001).
 - [74] O. Viyuela, D. Vodola, G. Pupillo, and M. A. Martin-Delgado, Topological massive dirac edge modes and long-range superconducting hamiltonians, *Phys. Rev. B* **94**, 125121 (2016).
 - [75] L. Lepori, D. Vodola, G. Pupillo, G. Gori, and A. Trombettoni, Effective theory and breakdown of conformal symmetry in a long-range quantum chain, *Annals of Physics* **374**, 35 (2016).
 - [76] U. Bhattacharya and A. Dutta, Topological footprints of the Kitaev chain with long-range superconducting pairings at a finite temperature, *Phys. Rev. B* **97**, 214505 (2018).
 - [77] D. Vodola, L. Lepori, E. Ercolessi, A. V. Gorshkov, and G. Pupillo, Kitaev chains with long-range pairing, *Phys. Rev. Lett.* **113**, 156402 (2014).
 - [78] A. Altland and M. R. Zirnbauer, Nonstandard symmetry classes in mesoscopic normal-superconducting hybrid structures, *Phys. Rev. B* **55**, 1142 (1997).

- [79] J. Zak, Berry's phase for energy bands in solids, *Phys. Rev. Lett.* **62**, 2747 (1989).
- [80] S. Tewari and J. D. Sau, Topological invariants for spin-orbit coupled superconductor nanowires, *Phys. Rev. Lett.* **109**, 150408 (2012).
- [81] L. Lepori and L. Dell'Anna, Long-range topological insulators and weakened bulk-boundary correspondence, *New Journal of Physics* **19**, 103030 (2017).
- [82] P. Phillips and H.-L. Wu, Localization and its absence: A new metallic state for conducting polymers, *Science* **252**, 1805 (1991).
- [83] N. M. Gergs, L. Fritz, and D. Schuricht, Topological order in the Kitaev/Majorana chain in the presence of disorder and interactions, *Phys. Rev. B* **93**, 075129 (2016).
- [84] P. H. Guimarães, G. T. Landi, and M. J. de Oliveira, Nonequilibrium quantum chains under multisite Lindblad baths, *Phys. Rev. E* **94**, 032139 (2016).
- [85] A. Nava, M. Rossi, and D. Giuliano, Lindblad equation approach to the determination of the optimal working point in nonequilibrium stationary states of an interacting electronic one-dimensional system: Application to the spinless Hubbard chain in the clean and in the weakly disordered limit, *Phys. Rev. B* **103**, 115139 (2021).
- [86] H.-P. Breuer and F. Petruccione, *The Theory of Open Quantum Systems* (Oxford University Press, 2007).
- [87] U. Weiss, *Quantum Dissipative Systems*, 5th ed. (World Scientific, 2021) <https://www.worldscientific.com/doi/pdf/10.1142/12402>.
- [88] J. Nilsson, A. R. Akhmerov, and C. W. J. Beenakker, Splitting of a cooper pair by a pair of Majorana bound states, *Phys. Rev. Lett.* **101**, 120403 (2008).
- [89] D. Guerzi and A. Nava, Probing Majorana zero modes by measuring transport through an interacting magnetic impurity, *Physica E: Low-dimensional Systems and Nanostructures* **134**, 114895 (2021).
- [90] I. Affleck and D. Giuliano, Topological superconductor–Luttinger liquid junctions, *Journal of Statistical Mechanics: Theory and Experiment* **2013**, P06011 (2013).
- [91] I. Affleck and D. Giuliano, Screening clouds and Majorana fermions, *Journal of Statistical Physics* **157**, 666 (2014).
- [92] E. G. Cinnirella, A. Nava, G. Campagnano, and D. Giuliano, Phase diagram of the disordered kitaev chain with long-range pairing connected to external baths, 10.5281/zenodo.15221285 (2025).